ADVANCED ELECTRONIC MATERIALS
www.advelectronicmat.de

Probing Ferrimagnetic Semiconductor with Enhanced Negative Magnetoresistance: 2D Chromium Sulfide

*Mohamad G. Moinuddin, Srikant Srinivasan, and Satinder K. Sharma**

Magnetic 2D materials have emerged as a great interest in spintronics due to atomic thickness scaling, low energy switching, and ease in the manipulation of spins. This report demonstrates a facile, bottom-up, chemical vapor deposition approach for non-van der Waals (non-vdWs), 2D chromium (III) sulfide (Cr_2S_3) with *c*-axis orientation, out-of-plane magnetic anisotropy (easy axis), and ferrimagnetic ordering. Importantly, the anisotropic magnetic saturation and resistivity of 10.23 mΩ cm reveal a narrow bandgap ferrimagnetism in Cr_2S_3 ($\Delta E_{Activation} \approx 22$ meV and $E_g \approx 40$ meV). The prototype lateral spin-channel Al/Cr_2S_3/Al devices exhibit a negative magnetoresistance of ≈25% and ≈15% at 100 K (below Néel temperature) for few-layer (≈8 nm) and thin-film (≈50 nm) device structures, respectively, owing to itinerant ferrimagnetism of Cr_2S_3. The magnetic field-induced spin polaron formations are quite resilient and enhance the field-dependent carrier conduction, making it greatly useful for negative magnetoresistance operation. These prototype Al/Cr_2S_3/Al structures have demonstrated a low power (≈2 µW for 8 µm channel at 10 µA current) operation with a negative field-dependent resistance coefficient (r_M) of ≈-5×10^{-4} Oe^{-1}. The computed r_M magnitude is tenfold higher than the bulk Cr_2S_3. This study identifies the potential of non-vdW Cr_2S_3 toward new and robust 2D-based spintronic applications.

Atomically thin, layered non-van der Waals (non-vdW) 2D magnetic materials have opened a new path to study energy-efficient device structures, new functionalities, and its potential applications in spintronics.[1,2] The advantage of 2D-based spintronics, contrary to conventional one, is to push the device scaling limit by using material engineering, mechanical flexibility, facile electrical, and chemically tunability.[1,3] Further, 2D non-vdW magnetic materials have shown great attention owing to strong variation in properties depending on the number of layers and large magnetic ordering near room temperature (RT). Still, there are limited investigations on non-vdWs systems owing to the inherent interlayer covalent bonding or columbic interaction that largely restricts the existence of ultrathin materials.[4] Lately, atomically thin non-vdW solids, including metal oxides (Fe_2O_3),[5] metal chalcogenides (EuS, FeS, $MnSe_x$),[6] and intermetallic (PtTe)[7] comprising spin and valley degree of freedom have been reported.[8] However, the theoretical predictions of 2D spintronic devices and circuits have been realized experimentally with the evolution of chromium (Cr)-based tri-halides (CrX_3; X = Cl, I, and Br).[9–17] More recently, CrI_3 and $CrCl_3$ with intrinsic magnetism have been introduced and incorporated into artificial heterostructures, possible applications include magnetic tunnel junction, read head sensors, and spin-FET.[16,18] Cai et al. have reported the field-induced negative magnetoresistance $\left(\mathrm{MR}(H) = \frac{R(H_{ext}) - R(0)}{R(0)}\right)$ of ≈36% in $CrCl_3$ with ultralow power operation at 1–15 mV (H_{ext} = 15 kOe and temperature = 2 K), where H_{ext} is applied field and R is resistance with and without field.[19] Besides this, the observed magnetic transitions in CrX_3 are found as CrI_3: 46 K, $CrBr_3$: 37 K, and $CrCl_3$: 17 K and hinders its applications owing to low-temperature magnetic ordering.[13] First-principles studies suggest that chromium-based chalcogenides CrM (M = S, Se, and Te) and CrMX may possess magnetic ordering higher than its halide with large energy band dissimilarity around the Fermi edge and offer a better spin transport in contrast to counterpart.[13] In this regard, chromium sulfide (Cr_2S_3) might be considered as a possible ferrimagnetic semiconductor[20,21] with mild resistivity (1–20 mΩ cm) and suitable for low power logic and nonvolatile application.[11,22–25] Naturally, the bulk ferrimagnetic Cr_2S_3 shows two crystal geometry: rhombohedral structure (R-3) with magnetization (3 emu mol^{-1}) and the other is trigonal structure (P-31c) with very low magnetization (7.2×10^{-3} emu mol^{-1}).[26] The rhombohedral Cr_2S_3 shows maximum values of 9% MR(H) in H_{ext} = 90 kOe at Neil temperature ($T_N \approx 120$ K). In contrast, the trigonal Cr_2S_3 sample shows negative magnetoresistance in which absolute values remain lower than 0.5% in 9 T independently of the temperature. Hence, for low-dimensional spin channel device structures R-3 Cr_2S_3 should be realized.[26]

In parallel to the immense efforts on device application, there is great interest in discovering suitable growth methods of magnetic compounds with high magnetic ordering temperatures. Driven by this, few non-vdW Cr-based magnetic materials ($Cr_2Ge_2Te_6$,[27] CrGe[28]) growth are reported through complex thin-film process, i.e., molecular beam epitaxy. On the other hand, chemical vapor deposition (CVD) techniques

M. G. Moinuddin, Dr. S. Srinivasan, Dr. S. K. Sharma
School of Computing and Electrical Engineering (SCEE)
Indian Institute of Technology (IIT)
Mandi, Himachal Pradesh 175075, India
E-mail: satinder@iitmandi.ac.in

The ORCID identification number(s) for the author(s) of this article can be found under https://doi.org/10.1002/aelm.202001116.

DOI: 10.1002/aelm.202001116

have also shown the new possibility for low-cost, high-purity, ultrathin 2D non-vdW growth.[29] Chu et al.[20] have reported the CVD growth of ferrimagnetic CrS_x nanosheets in the sub-millimeter range. More recently, enhanced electrical conduction with increasing thickness of CVD grown Cr_2S_3 is reported in detail.[21] It is also expected that while increasing the thickness of grown Cr_2S_3, the critical measure of magnetic ordering gets influenced by intralayer (compensated ferromagnetic) and interlayer (antiferromagnetic) anisotropy[30] and can be fine-tuned using an external magnetic field (H_{ext}) as stated by Yuzuri and Yoji.[23] Therefore, the development of a facile, restrained, and batch producible synthetic route is in high demand. In this work, we demonstrate the facile CVD growth of atomically, few layers, and thin Cr_2S_3 films over sapphire (Al_2O_3). Raman investigations show the availability of active modes in the nanoscale few-layer (staking of few monolayers) as well as thin-film Cr_2S_3. The magnetic analysis confirms the ferrimagnetic behavior considerable magnetic saturation and easy-axis anisotropy. The MR(H) characteristics of Al/Cr_2S_3/Al lateral device structures have opened up the understanding of a large negative MR under the external magnetic field (H_{ext}), which attribute to the intrinsic magnetic response of Cr_2S_3 and suggest new possibilities for low-dimensional systems for spintronics applications.

The nanoscale Cr_2S_3 was synthesized using a facile CVD with anhydrous chromium (II) chloride ($CrCl_2$) and sulfur (S) as precursors over sapphire (Al_2O_3-0001) substrate. At first, few-layer Cr_2S_3 were synthesized at 1123 K (850 °C) for 15 min growth duration. With the parameter explained in Table S1 (Supporting Information). Further, the layered thin films of Cr_2S_3 were synthesized when growth temperature and carrier gas (Ar:H_2) were kept constant and growth duration was increased to 0.5 h at 300 sccm (for 50 mm diameter reactor). The detailed facile synthesis approach has been shown in **Figure 1**a,b and Figures S1 and S2 (Supporting Information). The surface morphology of the single-crystal flake shows hexagonal edges owing to directional growth.[31] Figure 1d shows the atomic force microscopy images of few-layer samples with ≈8 nm thicknesses which correspond to the ≈5 monolayers of Cr_2S_3.[32,33] The X-ray diffraction (XRD) spectra suggest the single-crystal *c*-plane growth with rhombohedral geometry (R-3) as shown in Figure 1c,e. Three visible diffraction peaks of (003), (006), and (0012) are visible, in-line with the standard rhombohedral Cr_2S_3 structure (PDF No. 10-0340). The few-layer spectra (blue) show the major peaks available for the *c*-axis grown materials, some peaks could be merged or collapsed with the substrate intensity owing to their thickness. Moreover, in the thin-film case, peaks are more prominent due to sample volume. Some extra peaks are visible in thin-film spectra (black), but the spectral intensity ratio is less than 0.2× with respect to major *c*-axis. It justifies the monotonic growth in the few-layer flake-like crystal as well as thin film. To ensure well-controlled and consistent growth conditions, rectangle-shaped samples with 3–4 mm were diced and subjected to the micro-Raman spectroscopy for structural and X-ray photoelectron spectroscopy (XPS) for chemical analysis.[20]

It is evident from Figure 1f that two apparent Raman peaks are observed at 253.4 (E_g) and 286.21 (A_g) cm^{-1} for Cr_2S_3 with different thicknesses of ≈8 nm (few layers: blue) and ≈50 nm (thin film: black).[20] It is also noticeable that underneath the Al_2O_3 substrate signature at 410 cm^{-1} is not visible in the thin-film sample (black) due to higher thickness, but all signature modes available in the few-layer Cr_2S_3 are also evident in the thin-film sample. It confirms the consistent layered growth of Cr_2S_3 structures. These peaks positions have matched well with the available literature for 1T′ phase Cr_2S_3. A summary table of all Raman peaks and its comparison with literature is shown in Table S2 and Figure S3 (Supporting Information). Furthermore, these few-layer Cr_2S_3 has been mapped for Ag peak at 286.1 cm^{-1} and mapped flake has been shown in Figure 1g. The same flake structure has been investigated under energy dispersive spectroscopy (EDS) for chemical composition analysis and atomic ratio of Cr:S were observed as 6.67:9.99 (2:3). The detailed mapping is presented in Figure S4 (Supporting Information). Further, the XPS results in Figure 1i,j validate the pristine phase of Cr_2S_3 without oxidation and inclusion of any foreign material entity (Figure S5, Supporting Information). These results further evidently establish good stability in the air even after synthesis aging (data collected day of growth and after 30 d of the vacuum-sealed environment and shown in Figures S5 and S6, Supporting Information). Additionally, the $2p_{1/2}$ and $2p_{3/2}$ states of Cr are confirmed from the peaks at binding energies ≈583.8 and 574.9 eV (Figure 1i), whereas the peaks at binding energies ≈162.4 and 161.2 eV (Figure 1j) are meant for $2p_{1/2}$ and $2p_{3/2}$ states of sulfur (S), respectively. Interestingly, the peak fitted core spectra of Cr suggest the availability of low binding energy Cr (blue peak at 574.1 eV inside) the Cr_2S_3 which attributes the unbounded Cr, also explained by Cui et al.[21] Furthermore, valance band (VB) spectra were investigated to understand the electronic structure of Cr_2S_3 thin film. A helium source with 21.2 eV energy was used. These spectra exhibit a VB offset of nearly 0 eV which can indicate either that the Cr_2S_3 is a heavily doped p-type semiconductor or metallic.[34] As 1T′ Cr_2S_3 is a narrow bandgap semiconductor (NB-SC) with ≈36 meV and the synthesized Cr_2S_3 film shows only 1T′ phase in Raman, the narrow bandgap semiconductor interpretation of VB spectra is acceptable here. This NB-SC nature is further confirmed with the temperature-dependent resistivity analysis (shown later in Figure 3c). With evidence of structural and chemical measurements, the grown few-layer and thin-film Cr_2S_3 were subjected to magnetization analysis.

To quantify the Cr_2S_3 magnetic behavior, temperature-dependent SQUID-VSM (quantum design) analyses were performed. These investigations showed an interesting phenomenon of magnetic ordering (second order) with the probabilistic construction of paramagnetic → weak ferromagnetic or ferrimagnetic ordering as exhibited in the magnetization–field–temperature (*M*–*H*–*T*) curves of **Figure 2**. The *MHT* curve was plotted for the few-layer Cr_2S_3 with the magnetic field of ±5 kOe in the temperature range 300–10 K. Figure 2a,b shows the *MHT* for in-plane and out-of-plane magnetic field. The detailed *MH* for these contour plots are presented in Figures S7 and S8 (Supporting Information). From Figure 2c/d, the temperature ≈100 K may be considered as Néel point (T_N) similar to the bulk single crystals.[35] Based on *M*–*T* investigation, it is found that the in-plane and out-of-plane magnetization are not similar which suggests a sign of anisotropic behavior. A similar trend can also be observed when *M*–*T* is analyzed in μ_B/Cr atom which suggests that for small H_{ext} (500 Oe) magnetic dipoles are aligned toward out-of-plane. It can be explained as out-of-plane easy axis where two consecutive dipoles are aligned

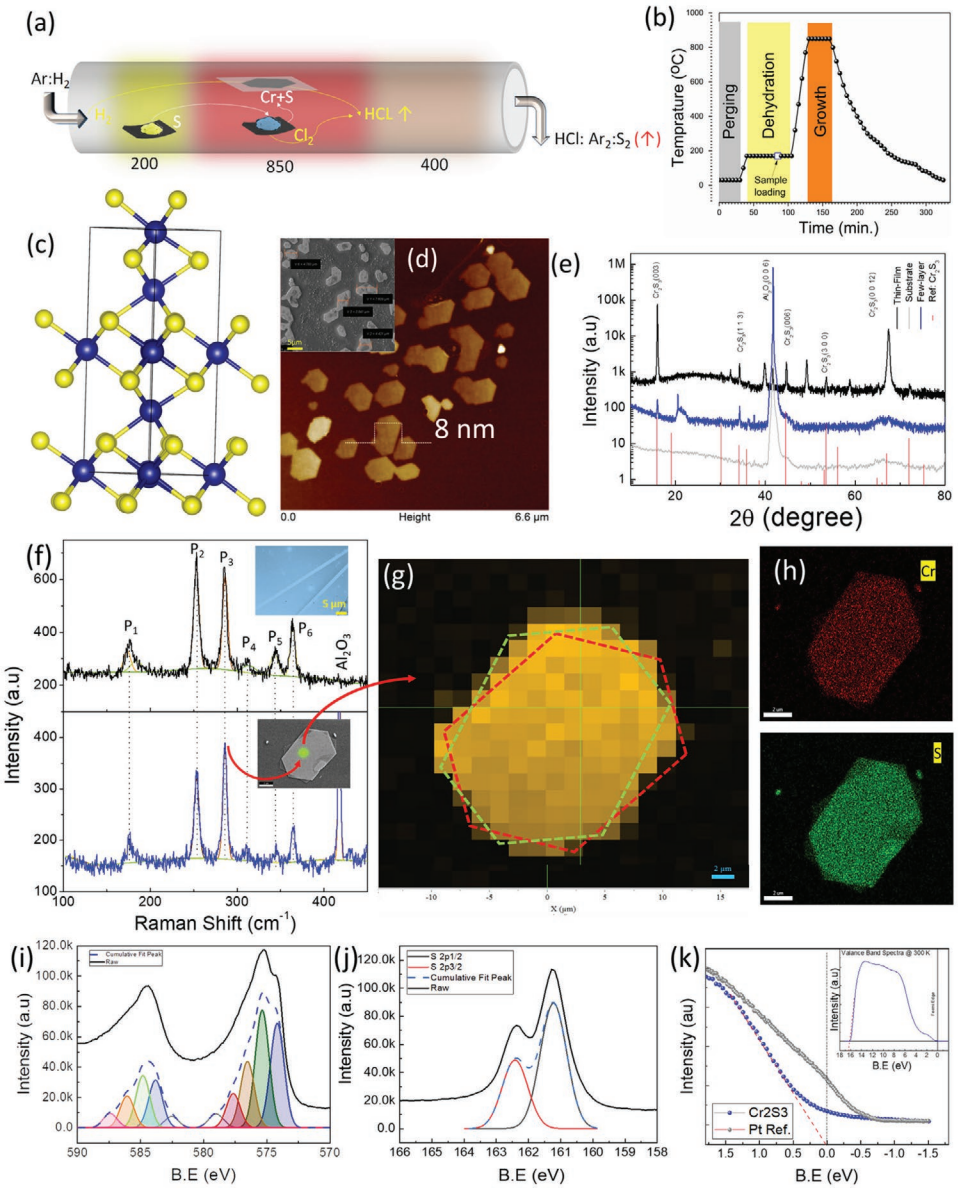

Figure 1. a) Growth schematic of Cr_2S_3 on sapphire using facile chemical vapor deposition (CVD); b) the temperature-growth kinetics is explained in time domain graph; c) crystal structure of grown Cr_2S_3 plotted with ICDD.CIF file; d) atomic force microscopy image of grown 2D Cr_2S_3 flakes, the inset shows large number of uniform flakes, the inset shows the grown Cr_2S_3 in layered geometry; e) XRD spectra for few-layer (down) and thin-film (up) samples and compared with the reference PCPDF 10-0340; f) micro-Raman analysis of synthesized 2D active modes; g) Raman mapping of 2D flake with Ag peak at 286.1 cm^{-1}; the mapping depicts the hexagonal structure and its properties; h) EDS mapping of same geometry for elemental analysis, EDS were done at low energy (7 keV) to avoid any damage due to long e-beam exposure; i,j) peak-fitted XPS core spectra of Cr 2p and S 2p, respectively. k) Further, valance band spectra in thin film were investigated and compared with metallic Pt thin film.

in opposite direction toward out-of-plane in FiM ordering. A possible spin schematic in Cr_2S_3 is visualized as Figure 2e, and a more detailed quantitative study is required for anisotropic application. However, to realize anisotropy qualitatively, region 2 from Figure 2c/d has been selected where maximum change in magnetization has been recorded near 100 K. So the *MH* data at 100 K clearly show two distinct magnetization path for the same Cr_2S_3 sample when it kept in-plane ($H\|$) and out-of-plane ($H\perp$) as shown in Figure 2f. The anisotropy field (H_k) was calculated from the point of overlap in normalized magnetization saturation for both fields ($H\|$ and $H\perp$). The H_k for 100 K was 1.83 kOe as shown in Figure 2f.

Based on the *M–H* analysis, the lateral channel prototype Al/Cr_2S_3/Al devices were fabricated with Cr_2S_3 as an active layer. The grown Cr_2S_3 over Al_2O_3 was patterned through standard semiconductor process flow and afterward, ≈40 nm non-magnetic aluminum (Al) was deposited using high vacuum thermal evaporation (fabrication process: Table S5 and Figure S9, Supporting Information).[36] The current–voltage (*J–V*) and resistance–temperature (ρ–*T*) analysis were investigated for

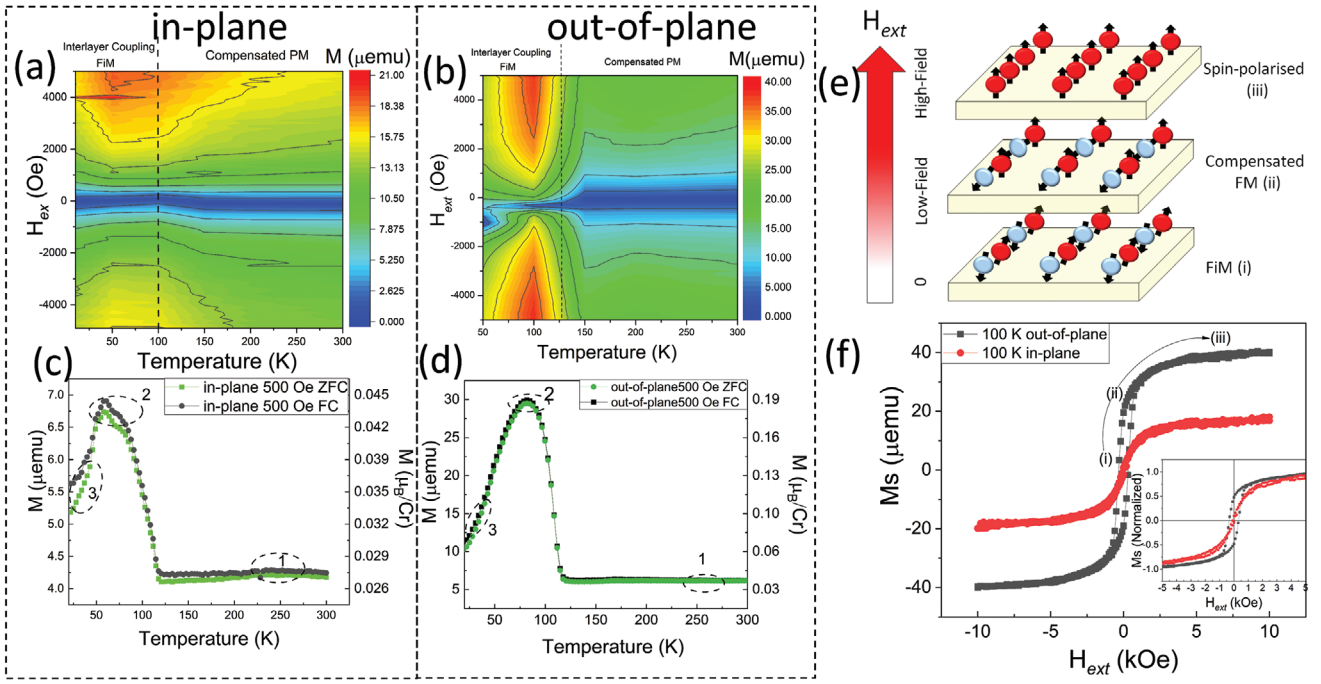

Figure 2. SQUID-based contour plots for the *M–H–T* curve show magnetization (μemu) for Cr_2S_3 and the absolute value magnetization scale were taken for clear understanding under a) in-plane ($H\|$) and b) out-of-plane ($H\perp$). *M–T* data for small field of 500 Oe in ZFC and FC condition, c) the in-plane data show minimal change in the magnetization, whereas d) out-of-plane shows a change with temperature, these *M–T* also found in-line with literature in table, e) schematic of domain alignment with the H_{ext}, considering the grown Cr_2S_3 are in out-of-plane easy axis. f) *M–H* plot for 100 K < T_N where the system is considered in spin-polarized condition.

Al/Cr_2S_3/Al structures (**Figure 3**a) in the absence of the applied magnetic field (H_{ext}). Figure 3b represents the *J–V* characteristics of Al/Cr_2S_3/Al structures, where bilateral ohmic behaviors are observed for device structure in −500 → +500 mV bias at room temperature. It indicates that conductivity in thin film has been increased with respect to the few-layer devices and reveals that there may be physical grain boundaries inside the thin film. The amalgamation of these grain boundaries is found to decrease the resistance of polycrystalline Cr_2S_3. Cui et al.[21] have also detected a similar enhancement with the increase in the thickness of Cr_2S_3 and explained it as the increased number of excess Cr inside the lattice. The few-layer flake-like crystals could be considered the ideal case where intralayer conduction is through free charge carrier (p-type considered). These conducting carriers find small potential barrier as they travel to the interlayer conduction at a low bias (≈200 mV). As the voltage increase (so the electric field) it provides an ease to the interlayer conduction and results in enhanced conduction. However, these augmentations were visualized change in resistance for the applied bias and only 4% change was observed as shown in Figure 3b inset. The fabricated device structure was also analyzed by increasing temperature from 296 to 310 K. By increasing the temperature the *J–V* was found increased for the same bias regime as shown in Figure 3b. On the other hand, electrical conduction at given temperature possess similar behavior. Beyond that to assess the formation of the ohmic junction of Cr_2S_3, we further investigated with the van der Pauw method and observed resistivity (ρ) were 10.2 ± 0.1 mΩ cm at room temperature (Figure 3c). The NB-SC behavior was further confirmed with the effect of thermal energy over electrical transport (ρ–*T*). The decay in resistivity was observed while increasing the temperature (Figure 3d). The resistivity behavior, semiconductor near 50 K, showed an opposite slope in ρ near T_N and again become semiconducting above T_N. For paramagnetic ($T > T_N$), the activation energy was found at 22.4 meV (see explanation in Figure S11, Supporting Information). Furthermore, above room-temperature ρ–*T* shows similar conduction behavior until it get saturated near 450 K. The apparent variation of resistance changes with temperature $\left(\frac{d\rho}{dT}\right)$ were found to be negative and converged to 0 near 450 K ($kT \approx 38.85$ meV). It perceives the minimum resistance state at 450 K, i.e., NB-SC to metallic transition (Figure 3d). The above said investigation also supports the first principal investigation of magnetic Cr_2S_3 (E_g = 20–40 meV), where the spin–orbit coupling is considered by Chen et al.[32]

Figure 4 shows the $MR(H) = \frac{R(H_{ext}) - R(0)}{R(0)}$ in Al/Cr_2S_3/Al for two geometries: few layers and thin film. These samples were investigated in a constant current mode in the PPMS (quantum design), the magnetic field was varied in sweep mode from 0→50 kOe →0→−50 kOe→0→50 kOe. A small current of 10 μA was provided to avoid any local heating at low temperature. Figure 4a shows the MR(*H*) for a wide range of temperatures across the T_N (≈100 K) (*T* = 300, 200, 150, 100, and 50 K). The resistance change ($\Delta R(H)$) at 100 K was found to be 6000 and 700 Ω for few-layer and thin-film devices, respectively. These $\Delta R(H)$ have resulted in the MR(*H*) of −25% (Figure 4a)

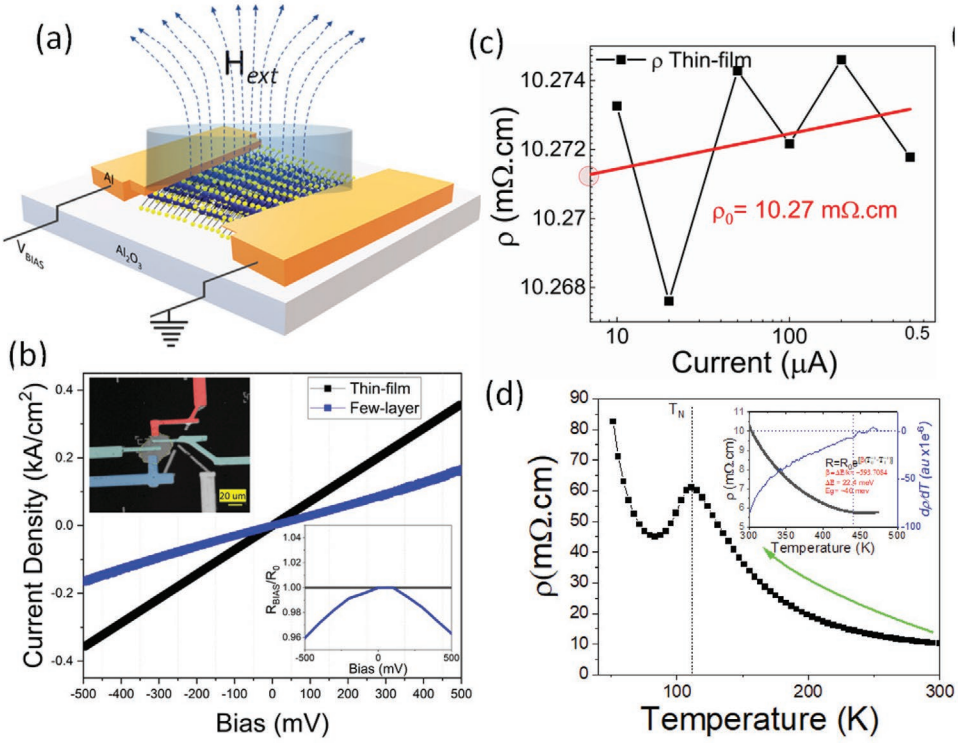

Figure 3. a) Schematic representation of current conduction in prototype Al/Cr_2S_3/Al lateral device; b) *J*–*V* measurements for few-layer and thin-film Al/Cr_2S_3/Al; J_C–*V* plot shows similar conduction in both geometry with certain current offset, inset shows bias-dependent resistance change; c) resistivity (ρ) of Cr_2S_3. d) Temperature dependence of the electrical resistivity (ρ) for a range of 50–450 K.

for few-layer and –15% (Figure 4b) for thin-film devices. As perceived from MH/MT investigation, the magnetization of Cr_2S_3 gets enhanced just below the T_N because the spins available inside the material are aligning to the weak ferromagnetic ordering. Cai et al. have also visualized similar conditions inside $CrCl_3$ and called it spin-polarized ordering.[19] Additionally, MR(*H*) at 50 K in both devices (7.55% and 5.8%) were found lower than the MR(*H*) at100 K. On the other hand, above T_N, the fabricated device structures had shown minimal MR(*H*) of ≈–1%. It suggests that the polarons inside Cr_2S_3 are responsive to the magnetic field, but the thermal disorders (*kT*) are dominant above T_N.[25]

Here, one can think quantitatively that how the same Cr_2S_3 can respond in two MR(*H*) by changing the thickness. To understand the difference in MR(*H*) in both devices, we can anticipate that the thin film may possess physical grain boundaries. The incorporation of grain boundaries suppresses the spin ordering and increases spin scattering near the boundaries (Figure S2, Supporting Information). The increased spin scattering decreases the MR(*H*).[49]

After a detailed study of MR(*H*) in both devices, the results were modeled with the existing theory of magnetic polaron hopping in magnetic semiconductors. As above said, it is expected that the available Cr inside the 2D lattice. These Cr ions act as carrier enriched polarons responsive to H_{ext}, i.e., a Cr^{2+} hopping polaron (see red in Figure 4e).[50] This large spin-induced conduction or decreased resistance $\Delta R(H)$ has been correlated with a polaron site-based hopping mechanism and explained Section S11 (Supporting Information). Further, as H_{ext} is applied, these Cr polaron sites create the localized magnetic alignment at a nanoscopic regime (M_S local due to polaron site) and act as polaron clouds, where nearby electrons get aligned toward the Cr spin and reduce the spin scattering. These H_{ext} enhance the majority spin-polarized conduction which results in high MR(*H*), also observed in 2D TiTeI system by Wu et al.[50,51] According to reported one, the field dependence of MR using the hopping mechanism by Lee et al.,[25] the MR(*H*) is a function of M_{ext}, thus proportional to M_{ext}^2 for $T > T_N$ and M_{ext} for $T < T_N$ in a low field region. However, for room-temperature investigations ($300 \gg T_N$), the *R*(*H*) decreases exponentially as evident from Figure 4d. When the polaron hopping hypothesis is considered, the correlation between *R*(*H*) and M_{ext} has been derived as follows

$$R(H) \propto e^{-A\left(\frac{M_{ext}}{M_0}\right)^2} \forall\, T > T_N \text{ and } R(H) \propto e^{-B\left(\frac{M_{ext}}{M_0}\right)} \forall\, T \le T_N \quad (1)$$

where M_{ext}, M_0, and *A* and *B* are field-induced magnetizations, zero fields spontaneous magnetization, and the proportionality constant, respectively.[25] Similarly, N_0 and N_{ext} are the net spins contributing to magnetization at zero field and external field in Cr_2S_3.[52] Here, the N_{ext} computed net spins contributing to the enhanced conduction is explained as follows

$$N_{ext} = \frac{N_{ext}}{V} = \frac{M_{ext}}{\mu_B} = \frac{M_{ext}}{\mu_o\left(1 + \frac{dM_{ext}}{dH}\right)} \quad (2)$$

where all acronyms are in standard form.

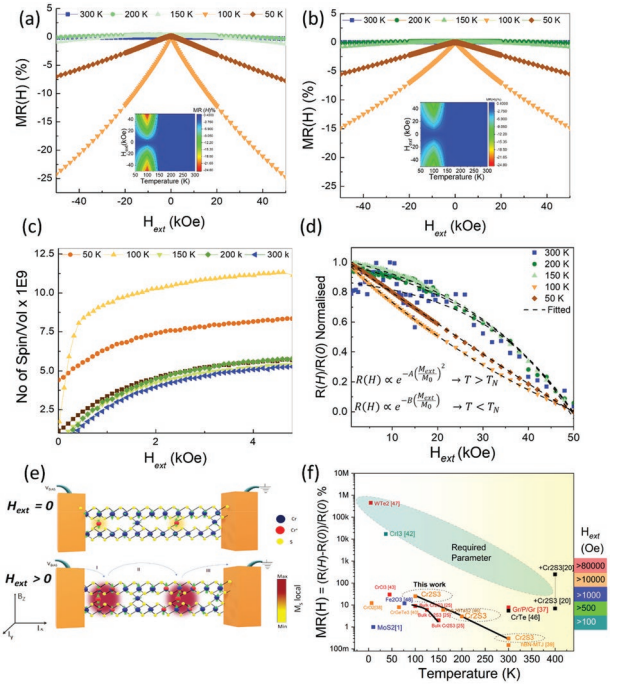

Figure 4. MR(H) investigation for Cr_2S_3 across the perpendicular external magnetic field. MR(H) of a) few-layer and b) thin-film Cr_2S_3 for ±50 kOe, c) net spins calculated from M–H virgin curve using Equation (3), d) modeled the MR(H) behavior with the applied field for different temperatures found in-line with Equation (2). e) Representation of polaron formation when Cr^+ is available inside the material, in absence of H_{ext} it aligns the nearby spins to reduce the magnetostatic energy of Cr_2S_3 and when H_{ext} is applied in easy axis, results in larger polaron site which helps in better conduction as shown in down. f) Summary of the figure of merit and roadmap of 2D magnetoresistive devices (detailed data are tabulated in Table S6, Supporting Information); the number denotes the references of earlier reported 2D materials.[1,19,37–48]

The experimental data were fitted with Equation (1) and shown in Figure 4d. The MR(H) was normalized to its maximum value to compare all the MR(H) as a function of H_{ext} and T. Mainly Figure 4d shows two types of slopes: linear for $T \leq T_N$ and nonlinear parabolic for $T > T_N$. The MR(H) is shown the same path at different temperatures, i.e., 300, 200, and 150 K, which can be justified with the available net spins at these temperatures as shown in Figure 2c. Similarly, for 100 and 50 K, the MR(H) path is linear which supports the polaron-based conduction [Equation (2)]. Considering the absolute value of MR(H), Figure 2c shows higher number of spin at 100 K with respect to 50 K, hence it also provided higher MR(H).

For the potential magnetoresistive device applications, the distinguishable resistance state and endurance investigations are imperative. The magnetic response of prototype Al/Cr_2S_3/Al devices with $\perp H_{ext}$ results in a significant change in resistance and can be quantized as the resistance state corresponds to desecrate field (H_{ext}) as shown in Figure 4a,b.[53] Regarding this, the magnetoresistive coefficient (r_M) has been calculated from the empirical relation for Al/Cr_2S_3/Al devices from $R(H)$ as $R(0)(1+r_M H_{ext}+e^{-\beta((T_0^{-1}-T_1^{-1})})$. Here, $\beta = \Delta E/K$ denotes a temperature coefficient of the electrical resistance value. During constant temperature analysis, β can be neglected and the simplified r_M is as follows

$$r_M = \frac{R(H)-R(0)}{R(0)\times H_{ext}} \quad (3)$$

The calculated r_M of ≈-5×10^{-4} Oe^{-1}, for spin-polarized condition at 100 K, offers a suitable 2D material similar to existing soft magnetic thin films.[54] The constant r_M behavior suggests the scope of MR extrapolation at a different field, such as ≈45% at the 90 kOe field as shown in Figure S12 (Supporting Information).

As unveiled in Figure 4f, the narrow bandgap semiconductor Cr_2S_3 channel devices with suitable growth engineering, may result in significant negative MR and resolve the critical issues of low-temperature magnetic ordering for 2D spintronics. It also exhibits more than ten times higher field sensitivity (r_M) and robust stability than the bulk Cr_2S_3, which are promising for low-power and high-performance spintronic device applications. In conclusion, the ferrimagnetic ordering of CVD grown 2D narrow bandgap ($\Delta E_{Activation} \approx 22.4$ meV; $\rho \approx 10.2$ mΩ cm) Cr_2S_3 were demonstrated at ≈100 K. Most importantly, the large negative MR up to −25% was observed in this grown 2D-Cr_2S_3, which is not usual in conventional semiconductors. As compared with other 2D-FMs, Cr_2S_3 preludes to low-power magnetoresistive sensors, advanced spin-FETs, and system-on-chip applications.

Associated Content

Besides these investigations, the authors observed robotic physical switching in Cr_2S_3 flake under the external magnetic field and recording shared in Video S1 (Supporting Information).

Supporting Information

Supporting Information is available from the Wiley Online Library or from the author.

Acknowledgements

The authors thank the C4DFED and AMRC centers at IIT Mandi, India for providing device fabrication, characterization, and materials characterization facilities; Dr. Kaustav Mukherjee and Dr. C. S. Yadav from IIT Mandi for assistance and discussion regarding SQUID-VSM study during the pandemic; M.G.M. was supported under the "Visvesvaraya Ph.D. Scheme" by MEiTY, India.

Conflict of Interest

The authors declare no conflict of interest.

Data Availability Statement

Research data are not shared.

Keywords

current–voltage characteristic, magnetic layered Cr_2S_3 materials, magnetoresistive devices, negative magnetoresistance, non-van der Waals growth

Received: November 13, 2020
Revised: June 9, 2021
Published online:

[1] W. Han, *APL Mater.* **2016**, *4*, 032401.
[2] K. S. Burch, D. Mandrus, J. G. Park, *Nature* **2018**, *563*, 47.
[3] Y. P. Feng, L. Shen, M. Yang, A. Wang, M. Zeng, Q. Wu, S. Chintalapati, C.-R. Chang, *WIREs Comput. Mol. Sci.* **2017**, *7*, e1313.
[4] X. Sun, Z. Chen, Y. Wang, Z. Lu, J. Shi, M. Washington, T.-M. Lu, *J. Appl. Phys.* **2018**, *123*, 025303.
[5] A. P. Balan, S. Radhakrishnan, C. F. Woellner, S. K. Sinha, L. Deng, C. D. L. Reyes, B. M. Rao, M. Paulose, R. Neupane, A. Apte, V. Kochat, R. Vajtai, A. R. Harutyunyan, C. W. Chu, G. Costin, D. S. Galvao, A. A. Martí, P. A. Van Aken, O. K. Varghese, C. S. Tiwary, A. M. M. R. Iyer, P. M. Ajayan, *Nat. Nanotechnol.* **2018**, *13*, 602.
[6] I. S. Sokolov, D. V. Averyanov, O. E. Parfenov, I. A. Karateev, A. N. Taldenkov, A. M. Tokmachev, V. G. Storchak, *Mater. Horiz.* **2020**, *7*, 1372.
[7] R. A. B. Villaos, C. P. Crisostomo, Z.-Q. Huang, S.-M. Huang, A. A. B. Padama, M. A. Albao, H. Lin, F.-C. Chuang, *NPJ 2D Mater. Appl.* **2019**, *3*, 2.
[8] D. Sander, S. O. Valenzuela, D. Makarov, C. H. Marrows, E. E. Fullerton, P. Fischer, J. McCord, P. Vavassori, S. Mangin, P. Pirro, B. Hillebrands, A. D. Kent, T. Jungwirth, O. Gutfleisch, C. G. Kim, A. Berger, *J. Phys. D: Appl. Phys.* **2017**, *50*, 363001.
[9] C. Wang, X. Zhou, L. Zhou, N. H. Tong, Z. Y. Lu, W. Ji, *Sci. Bull.* **2019**, *64*, 293.
[10] J. Zhou, J. Qiao, C. G. Duan, A. Bournel, K. L. Wang, W. Zhao, *ACS Appl. Mater. Interfaces* **2019**, *11*, 17647.
[11] P. Vaqueiro, A. V. Powell, A. I. Coldea, C. A. Steer, I. M. Marshall, S. J. Blundell, J. Singleton, T. Ohtani, *Phys. Rev. B: Condens. Matter Mater. Phys.* **2001**, *64*, 1324021.
[12] M. Gibertini, M. Koperski, A. F. Morpurgo, K. S. Novoselov, *Nat. Nanotechnol.* **2019**, *14*, 408.
[13] Z. Jiang, P. Wang, J. Xing, X. Jiang, J. Zhao, *ACS Appl. Mater. Interfaces* **2018**, *10*, 39032.
[14] Y. Liu, L. Wu, X. Tong, J. Li, J. Tao, Y. Zhu, C. Petrovic, *Sci. Rep.* **2019**, *9*, 13599.
[15] M. Abramchuk, S. Jaszewski, K. R. Metz, G. B. Osterhoudt, Y. Wang, K. S. Burch, F. Tafti, *Adv. Mater.* **2018**, *30*, 1801325.
[16] S. Jiang, L. Li, Z. Wang, K. F. Mak, J. Shan, *Nat. Nanotechnol.* **2018**, *13*, 549.
[17] H. Moulkhalwa, Y. Zaoui, K. O. Obodo, A. Belkadi, L. Beldi, B. Bouhafs, *J. Supercond. Novel Magn.* **2019**, *32*, 635.
[18] C. Cardoso, D. Soriano, N. A. García-Martínez, J. Fernández-Rossier, *Phys. Rev. Lett.* **2018**, *121*, 067701.
[19] X. Cai, T. Song, N. P. Wilson, G. Clark, M. He, X. Zhang, T. Taniguchi, K. Watanabe, W. Yao, D. Xiao, M. A. McGuire, D. H. Cobden, X. Xu, *Nano Lett.* **2019**, *19*, 3993.
[20] J. Chu, Y. Zhang, Y. Wen, R. Qiao, C. Wu, P. He, L. Yin, R. Cheng, F. Wang, Z. Wang, J. Xiong, Y. Li, J. He, *Nano Lett.* **2019**, *19*, 2154.
[21] F. Cui, X. Zhao, J. Xu, B. Tang, Q. Shang, J. Shi, Y. Huan, J. Liao, Q. Chen, Y. Hou, Q. Zhang, S. J. Pennycook, Y. Zhang, *Adv. Mater.* **2020**, *32*, e1905896.
[22] A. Maignan, Y. Bréard, E. Guilmeau, F. Gascoin, *J. Appl. Phys.* **2012**, *112*, 013716.
[23] M. Yuzuri, N. Yoji, *J. Phys. Soc. Jpn.* **1964**, *19*, 1350.
[24] K. Singh, A. Maignan, C. Martin, C. Simon, *Chem. Mater.* **2009**, *21*, 5007.
[25] K. D. Lee, C. J. Won, K. M. Song, N. Hur, *J. Appl. Phys.* **2011**, *109*, 063906.
[26] A. Koizumi, J. Suda, T. Kimoto, *J. Appl. Phys.* **2015**, *106*, 013716.
[27] M. Mogi, A. Tsukazaki, Y. Kaneko, R. Yoshimi, K. S. Takahashi, M. Kawasaki, Y. Tokura, *APL Mater.* **2018**, *6*, 091104.
[28] A. S. Ahmed, B. D. Esser, J. Rowland, D. W. McComb, R. K. Kawakami, *J. Cryst. Growth* **2017**, *467*, 38.
[29] Z. Cai, B. Liu, X. Zou, H. M. Cheng, *Chem. Rev.* **2018**, *118*, 6091.
[30] A. Bandyopadhyay, N. C. Frey, D. Jariwala, V. B. Shenoy, *Nano Lett.* **2019**, *19*, 7793.
[31] S. Zhou, R. Wang, J. Han, D. Wang, H. Li, L. Gan, T. Zhai, *Adv. Funct. Mater.* **2019**, *29*, 1805880.
[32] M. R. Habib, S. Wang, W. Wang, H. Xiao, S. M. Obaidulla, A. Gayen, Y. Khan, H. Chen, M. Xu, *Nanoscale* **2019**, *11*, 20123.
[33] J. Y. Chen, X. X. Li, W. Z. Zhou, J. L. Yang, F. P. Ouyang, X. Xiong, *Adv. Electron. Mater.* **2020**, *6*, 1900490.
[34] L. A. Walsh, R. Yue, Q. Wang, A. T. Barton, R. Addou, C. M. Smyth, H. Zhu, J. Kim, L. Colombo, M. J. Kim, R. M. Wallace, C. L. Hinkle, *2D Mater.* **2017**, *4*, 025044.
[35] T. Sugiura, K. Iwahashi, Y. Masuda, *J. Phys. Soc. Jpn.* **1972**, *33*, 1172.
[36] M. G. Moinuddin, A. H. Lone, S. Srinivasan, S. K. Sharma, *ACS Appl. Electron. Mater.* **2019**, *1*, 2268.
[37] Y. Liu, I. Yudhistira, M. Yang, E. Laksono, Y. Z. Luo, J. Chen, J. Lu, Y. P. Feng, S. Adam, K. P. Loh, *Nano Lett.* **2018**, *18*, 3377.
[38] M. S. Anwar, F. Czeschka, M. Hesselberth, M. Porcu, J. Aarts, *Phys. Rev. B: Condens. Matter Mater. Phys.* **2010**, *82*, 2.
[39] A. Dankert, M. V. Kamalakar, A. Wajid, R. S. Patel, S. P. Dash, *Nano Res.* **2015**, *8*, 1357.
[40] G. T. Lin, H. L. Zhuang, X. Luo, B. J. Liu, F. C. Chen, J. Yan, Y. Sun, J. Zhou, W. J. Lu, P. Tong, Z. G. Sheng, Z. Qu, W. H. Song, X. B. Zhu, Y. P. Sun, *Phys. Rev. B* **2017**, *95*, 245212.
[41] A. J. Littlejohn, Z. Li, Z. Lu, X. Sun, P. Nawarat, Y. Wang, Y. Li, T. Wang, Y. Chen, L. Zhang, H. Li, K. Kisslinger, S. Shi, J. Shi, A. Raeliarijaona, W. Shi, H. Terrones, K. M. Lewis, M. Washington, T. M. Lu, G. C. Wang, *ACS Appl. Nano Mater.* **2019**, *2*, 3684.
[42] H. H. Kim, B. Yang, S. Li, S. Jiang, C. Jin, Z. Tao, G. Nichols, F. Sfigakis, S. Zhong, C. Li, S. Tian, D. G. Cory, G. X. Miao, J. Shan, K. F. Mak, H. Lei, K. Sun, L. Zhao, A. W. Tsen, *Proc. Natl. Acad. Sci. USA* **2019**, *166*, 11131.
[43] D. R. Klein, D. MacNeill, J. L. Lado, D. Soriano, E. Navarro-Moratalla, K. Watanabe, T. Taniguchi, S. Manni, P. Canfield, J. Fernández-Rossier, P. Jarillo-Herrero, *Science* **2018**, *360*, 1218.
[44] X. Sun, W. Li, X. Wang, Q. Sui, T. Zhang, Z. Wang, L. Liu, D. Li, S. Feng, S. Zhong, H. Wang, V. Bouchiat, M. N. Regueiro, N. Rougemaille, J. Coraux, A. Purbawati, A. Hadj-Azzem, Z. Wang, B. Dong, X. Wu, T. Yang, G. Yu, B. Wang, Z. Han, X. Han, Z. Zhang, *Nano Res.* **2020**, *12*, 3358.
[45] I. A. Verzhbitskiy, H. Kurebayashi, H. Cheng, J. Zhou, S. Khan, Y. P. Feng, G. Eda, *Nat. Electron.* **2020**, *3*, 460.
[46] M. Arai, R. Moriya, N. Yabuki, S. Masubuchi, K. Ueno, T. Machida, *Appl. Phys. Lett.* **2015**, *107*, 103107.
[47] M. N. Ali, J. Xiong, S. Flynn, J. Tao, Q. D. Gibson, L. M. Schoop, T. Liang, N. Haldolaarachchige, M. Hirschberger, N. P. Ong, R. J. Cava, *Nature* **2014**, *514*, 205.
[48] Y. Masubuchi, M. Minoya, T. Takeda, S. Kikkawa, *J. Am. Ceram. Soc.* **2011**, *94*, 765.
[49] S. I. Rybchenko, Y. Fujishiro, H. Takagi, M. Awano, *Phys. Rev. B: Condens. Matter Mater. Phys.* **2005**, *72*, 054424.
[50] J. F. Wooos, C. Y. Chen, *Phys. Rev.* **1964**, *135*, A1462.
[51] A. Kaminski, S. D. Sarma, *Phys. Rev. B: Condens. Matter Mater. Phys.* **2003**, *68*, 235210.
[52] S. Datta, *Quantum Transport: Atom to Transistor*, Cambridge University Press, Cambridge **2005**.
[53] A. P. Ramirez, *J. Phys. Condens. Matter* **1997**, *9*, 8171.
[54] N. Kobayashi, T. Yano, S. Ohnuma, K. Shirakawa, T. Masumoto, *EP1329735B1* **2010**.